

1 **Greenhouse gas effects on the solar cycle response of water vapour and noctilucent**
2 **clouds**

3 Ashique Vellalassery¹, Gerd Baumgarten¹, Mykhaylo Grygalashvily¹, and Franz-Josef
4 Lübken¹

5 ¹Leibniz Institute of Atmospheric Physics at the University of Rostock, Schloßstraße 6, D-
6 18225 Kühlungsborn, Germany

7 *Correspondence to:* Ashique Vellalassery (ashique@iap-kborn.de)

8
9 **Abstract**

10
11 The response of water vapour (H₂O) and noctilucent clouds (NLCs) to the solar cycle are
12 studied using the Leibniz Institute for Middle Atmosphere (LIMA) model and the Mesospheric
13 Ice Microphysics And tranSPort (MIMAS) model. NLCs are sensitive to the solar cycle because
14 their formation depends on background temperature and the H₂O concentration. The solar cycle
15 affects the H₂O concentration in the upper mesosphere mainly in two ways: directly through
16 the photolysis and, in time and place of NLCs formation, indirectly through temperature
17 changes. We found that H₂O concentration correlates positively with the temperature changes
18 due to the solar cycle at altitudes above about 82 km, where NLCs form. The photolysis effect
19 leads to an anti-correlation of H₂O concentration and solar Lyman- α radiation, which gets even
20 more pronounced at altitudes below ~83 km when NLCs are present. We studied the H₂O
21 response to Lyman- α variability for the period 1992 to 2018, including the two most recent
22 solar cycles. The amplitude of Lyman- α variation decreased by about 40% in the period 2005
23 to 2018 compared to the preceding solar cycle, resulting in a lower H₂O response in the late
24 period. We investigated the effect of increasing greenhouse gases (GHGs) on the H₂O response
25 throughout the solar cycle by performing model runs with and without increases in carbon
26 dioxide (CO₂) and methane (CH₄). The increase of methane and carbon dioxide amplify the

27 response of water vapour to the solar variability. Applying the geometry of satellite
28 observations, we find a missing response when averaging over altitudes of 80 to 85 km, where
29 H₂O has a positive and a negative response (depending on altitude) which largely cancel out.
30 One main finding is that during NLCs the solar cycle response of H₂O strongly depends on
31 altitude.

32

33 **1. Introduction**

34

35 The 11-year solar cycle significantly influences the upper atmosphere's temperature and water
36 vapour (H₂O) concentration. H₂O is one of the essential minor constituents in the mesosphere
37 as it is the primary source of chemically active hydrogen radicals, influencing the chemistry of
38 all other chemically active minor constituents (Brasseur and Solomon, 2005, Hartogh et al.,
39 2010). H₂O concentration plays an essential role in the noctilucent cloud's (NLC) formation.
40 NLCs are located at about 83 km altitude, consist of water ice particles, and owe their existence
41 to the cold summer mesopause region (~130K) at mid and high latitudes. NLCs, also called
42 polar mesospheric clouds, are formed in an environment where small changes in background
43 H₂O and temperature can lead to significant changes in NLC properties (e.g., Thomas, 1996;
44 DeLand et al., 2006; Shettle et al., 2009, Lübken et al., 2009).

45 In comparison to the lower atmosphere, little is known about the upper mesosphere/lower
46 thermosphere (MLT, 75-110 km) due to a lack of observations at these altitudes. NLCs have
47 been proposed as indicators of trends in background temperature and H₂O concentrations
48 (Thomas & Olivero, 2001). Studying NLC properties provide insight in phenomena occurring
49 at the altitude of NLC. The 11-year solar cycle has been considered to cause quasi decadal
50 oscillation observed in NLCs (DeLand et al., 2003). NLCs are predicted to decrease during
51 solar maximum due to increased heating and photolysis of H₂O (Garcia, 1989). However, some
52 recent studies strongly suggest that the response of NLCs to the solar cycle has been absent

53 from 2002 to the present (Fiedler et al., 2011; DeLand & Thomas, 2015; Hervig et al., 2016;
54 Siskind et al., 2013). Hervig et al. (2019), using satellite observations, found that NLC had a
55 clear anti-correlation with the solar cycle before 2002, and that response has been absent in
56 recent years. The leading cause of this absence appears to be the suppression of the solar cycle
57 response of H₂O. Lyman- α (Ly α) radiation is the primary cause of H₂O photolysis and varies
58 by a factor of two between solar minimum and maximum (Woods et al., 2000). Understanding
59 the effects of the solar cycle on H₂O is more complicated at NLC altitudes because of the
60 interaction between NLCs and background H₂O.

61 NLC growth leads to dehydration at higher altitudes (83-89 km) as ice particles are formed by
62 consuming background H₂O, and sublimation of ice particles leads to hydration at lower
63 altitudes as H₂O is released here (about 78-83 km) (Lübken et al., 2009, Hervig et al., 2003).
64 Investigating the effects of NLC on the background H₂O requires an estimate of the H₂O profile
65 without NLCs. Investigations using satellite observations are limited due to uncertainty in the
66 inferred background H₂O without NLC and vertical resolutions in the order of a few 100~m.
67 Therefore, using satellite observations to study H₂O at NLC altitudes could yield misleading
68 results due to biases in the estimated H₂O profiles without NLC (Hervig et al., 2015). Hervig
69 et al. (2015) suggest that in future studies, one approach to investigate the effects of NLC on
70 H₂O would be to use a detailed microphysical NLC model. Therefore, for this study,
71 simulations are performed with and without microphysics using the same background
72 conditions, resulting in a H₂O profile with and without NLC. This allows us to investigate how
73 NLC formation changes the H₂O background profile in detail.

74 We compare the model result to satellite observations published by Hervig et al. (2019) to
75 investigate the mechanism behind the solar cycle response of NLC and H₂O. We also focus on
76 the missing solar cycle response of H₂O during recent years. This paper aims to answer a
77 number of questions: How does the formation of NLCs affect the H₂O profile and the variation
78 of water vapour with the solar cycle? How do the solar cycle-induced temperature and

79 photolysis changes affect the H₂O response? Why is the response of water vapour to solar cycle
80 nearly absent in satellite observations after 2005 (Hervig et al., 2019)? Our study is focused on
81 the core NLC period, i.e., July at 68±5°N. The following section describes the modelling
82 framework of this study and discusses the various model simulations performed. The third
83 section discusses the mechanisms behind the solar cycle H₂O response, such as the separation
84 of the solar cycle-induced temperature and photolysis effects on H₂O. Sections four and five
85 explore the possible reasons behind the missing solar cycle response. Concluding remarks and
86 a summary are given in the last section.

87

88 **2. Model description and numerical experiments**

89

90 **2.1. Model**

91

92 The modelling framework used in this study consists mainly of two components: the Leibniz
93 Institute Middle Atmosphere (LIMA) model and the Mesospheric Ice Microphysics And
94 tranSport (MIMAS) model (see Fig. 1). LIMA is a non-linear, global, 3D Eulerian grid-point
95 model reaching from the troposphere to the lower thermosphere, which calculates winds and
96 temperature and is well described in a number of papers (Berger, 2008; Lübken et al., 2013).
97 The LIMA model in this study is nudged to reanalysis data NOAA-CIRES (National Oceanic
98 and Atmospheric Administration-Cooperative Institute for Research in Environmental Sciences
99 20CR; Compo et al., 2011) up to an altitude of 45 km. The resulting winds and temperatures in
100 the mesosphere and lower thermosphere (MLT) are then used in MIMAS. The MIMAS model
101 run was performed for all years with background wind conditions and gravity wave forcing
102 from a representative year (1976).

103 MIMAS is a 3D Lagrangian transport model specifically designed for modelling ice particles
104 in MLT region (Berger and Lübken, 2015). MIMAS calculates NLC parameters from 10 May

105 to 31 August, and it is constrained from mid-latitudes to high latitudes (37° - 90° N) with a
106 horizontal grid resolution of 1° in latitude and 3° in longitude and a vertical resolution of 100
107 m from 77.8 to 94.1 km (163 levels). In this study, the dynamics calculated by LIMA, solar
108 $\text{Ly}\alpha$, and the initial H_2O distribution are the input for MIMAS as sketched in Figure 1. Below
109 the MIMAS lower boundary two effects determine the mixing ratio of H_2O in the stratosphere:
110 (i) transport of H_2O from the troposphere and (ii) oxidation of methane (CH_4). The oxidation
111 of each CH_4 molecule produces two H_2O molecules. Methane is nearly completely converted
112 to H_2O in the mesosphere by photochemical processes (e.g., Lübken et al., 2018). MIMAS
113 assumes that transport from the troposphere is constant. The increase in H_2O is primarily
114 through (ii) i.e. due to the increase in CH_4 concentration (Lübken et al., 2018). Then,
115 mesospheric H_2O in MIMAS is transported by background winds, dispersed by turbulent
116 diffusion, and reduced by photolysis. Hence, we parametrize H_2O as a function of CH_4
117 following by Lübken et al., 2018 (see Section 2). MIMAS makes use of 40 million dust
118 particles, which can act as condensation nuclei. Dust particles are formed from meteors
119 evaporating in the atmosphere (for more details, see Berger and von Zahn, 2002; von Zahn and
120 Berger, 2003, Killiani, 2014). These are then coated with ice in H_2O supersaturated regions and
121 transported according to three-dimensional and time-dependent background winds, eddy
122 diffusion, and sedimentation. In MIMAS, standard microphysical processes such as the Kelvin
123 effect determine the nucleation and growth of ice particles (Berger & Lübken, 2015; Gadsden
124 & Schröder, 1989). For the comparison with satellites, we used model run A, which includes
125 CO_2 and CH_4 variations (Lübken et al., 2018; Lübken et al., 2021). We performed MIMAS
126 model simulations with ice formation turned off and on respectively to investigate the effects
127 of ice formation on background H_2O . In both runs, the background conditions and model inputs
128 are the same. The main outputs of the model are the microphysical properties of the NLC ice
129 particles, such as radius, backscatter value, and the number density of the ice/dust particles.
130 More detailed descriptions of the MIMAS model and its precursors are available in the literature

131 (Berger and von Zahn, 2002; Berger, 2008; Berger and Lübken, 2011; Lübken et al., 2018;
132 Lübken et al., 2021).

133

134 **2.2. Model simulations**

135

136 LIMA and MIMAS use daily Ly α fluxes taken from the LASP Interactive Solar Irradiance Data
137 Center (LISIRD) as a proxy for solar activity from 1961 to 2019 (Machol et al. 2019). Ly α (and
138 other spectral bands) variations in LIMA cause atmospheric temperature variations, while Ly α
139 variations in MIMAS cause photolysis of H₂O. In LIMA, variation of other bands, namely,
140 Chappius band, Huggins band, Hartley band, Schumann-Runge band, and both Schumann-
141 Runge continuums are taken into account. The parametrization schemes are discussed in more
142 detail in Berger, 2008 (see Section 2.2). Variations of these bands are parametrized based on
143 Ly α values according to Lean et al. (1997). Therefore, it is possible to study the effects of solar
144 cycle on H₂O due to temperature changes and photolysis separately by performing model
145 simulations with constant and varying Ly α in MIMAS and LIMA. We conducted four model
146 runs, as described in Table 1. We also performed LIMA model simulations with constant CO₂
147 for runs E, F, and G to filter out their effects on temperature changes. For these runs we use a
148 constant CH₄ concentration in MIMAS to avoid its influence on the H₂O profile.

149 In LIMA, the mixing ratios of CO₂ (28-150 km) vary as function of time (years), while all other
150 trace gases are kept constant. An increase in CO₂ leads to a decrease in temperature in the
151 stratosphere mainly due to enhanced cooling by CO₂ (e.g., Roble and Dickinson, 1989; Garcia
152 et al., 2007; Berger & Lübken, 2011; Marsh et al., 2013; Lübken et al., 2013). At NLC altitudes,
153 this cooling leads to an altitude decrease of pressure levels, referred to as the ‘shrinking effect’
154 (Lübken et al., 2009). For LIMA we use the long-term increase of CO₂ concentration according
155 to observations at Mauna Loa (19°N, 155°W).

156 This study focuses mainly on the recent two solar cycles from 1992 to 2018. Figure 2 shows
157 the time series of Ly α , CO₂, and CH₄ for 1992-2018. The corresponding values of Ly α , CH₄,
158 and CO₂ for the years considered for this study are highlighted. We classify 1992-2005 as period
159 1 (“early”) and 2005-2018 as period 2 (“late”). Satellite observations of H₂O showed a clear
160 anti-correlation with the solar cycle in the early period, which was absent in the late period
161 (Hervig et al. 2019). Certainly, at low and middle latitudes, without NLCs one can detect only
162 anticorrelation. For example, in H₂O satellite data averaged over the tropics (30° N-30° S), anti-
163 correlation is observed for the "late" period (Karagodin-Doyennel et al. 2021). To investigate
164 the missing response reported in Hervig et al. 2019, we first examined the early period solar
165 minimum (1997) and maximum (2002) in more detail. The solar cycle affects the H₂O
166 concentration in two main ways. (i) through the photolysis of H₂O by Ly α , and (ii) through the
167 temperature effect. We distinguish these effects by performing model simulations with different
168 background conditions (see Table 1). Namely in section 3.3, we discuss the individual role of
169 solar cycle-induced photolysis and temperature change on the H₂O-solar cycle response. Figure
170 2 shows that the intensity of Ly α radiation during the late period has decreased compared to
171 the early period, and the concentrations of increased greenhouse gases (GHGs) have increased
172 in the late period. The effects of reduced Ly α intensity and increased greenhouse gas (GHG)
173 concentration on long-term H₂O-solar cycle response are discussed in section 4.

174

175 **3. Results and Discussions**

176

177 **3.1. Solar cycle response in ice water content (IWC)**

178

179 To determine if the model agrees with satellite observations, we compared the ice water content
180 (IWC) anomaly from the model with the satellite observations (see Fig. 3). IWC anomalies are
181 calculated as follows:

Fig. 3

$$182 \quad IWC_{anom} = 100\% \cdot \frac{\overline{IWC_{July}} - \overline{IWC_{1981-2018}}}{\overline{IWC_{1981-2018}}}, \quad (1)$$

183 Where $\overline{IWC_{July}}$ represent monthly zonal averages at 68°N, and $\overline{IWC_{1981-2018}}$ are the averages
184 of $\overline{IWC_{July}}$ over the years 1981-2018. The IWC anomaly for satellite measurements are from
185 the Solar Backscatter Ultraviolet (SBUV), Halogen Occultation Experiment (HALOE), Cloud
186 Imaging and Particle Size (CIPS), and Solar Occultation For Ice Experiment (SOFIE)
187 instruments. The time series of SBUV and HALOE data as shown in Figure 3 represent three
188 years sliding averaged values. For more details on the satellite datasets, see Hervig et al. (2019).
189 For this comparison, we used the MIMAS run A, in which the simulations are performed with
190 increasing concentrations of CO₂ and CH₄. For the comparison, we applied the same calculation
191 method to our model data as Hervig et al. (2019) did on satellite observations, namely, we used
192 a threshold of 50 g/km³ for integrated water content because the PMC detection threshold for
193 SBUV is 50 g/km³ (DeLand and Thomas, 2015, 2019).
194 We find an anti-correlation between MIMAS IWC anomaly and Ly α flux throughout the entire
195 period (1981-2018), with a weaker response in the late period. In satellite observations, SBUV
196 measurements also show an anti-correlation with Ly α flux until 2005, after which the response
197 becomes weaker in agreement with MIMAS. The magnitude of the solar cycle IWC anomaly
198 in SBUV and HALOE is of the same order as the IWC anomaly in MIMAS. The IWC anomalies
199 of CIPS and SOFIE do not show a clear response to the solar cycle. We notice that the year-to-
200 year IWC variation in CIPS and SOFIE is larger than the IWC modulation during a solar cycle.
201 IWC anomalies of SBUV and HALOE correlate well with MIMAS IWC anomalies before 2005
202 and progressively weaken afterwards. Lübken et al. (2009) found a good agreement between
203 NLC parameters calculated by MIMAS and satellite observations. The general agreement
204 between the main characteristics and trends of the ice layers in MIMAS and the observations
205 suggests that the microphysical and photochemical processes in MIMAS cover the main
206 processes relevant to NLC formation (Lübken et al., 2009).

207

208 3.2. Effect of NLC on water vapour (H₂O)

209

210 We calculated the zonal mean monthly averaged vertical profiles of H₂O and temperature to
211 investigate the impact of NLC formation on the H₂O profile. Figure 4 shows the vertical H₂O
212 profile averaged for July at 68°N latitude and given on pressure altitudes $z_p = H_p \ln(p_0/p)$.

Fig. 4

213 Where p is the pressure of the model level, p_0 is the pressure at the surface and $H_p = 7$ km is
214 the pressure scale height. This figure illustrates the effect of NLC formation on the background
215 profile of water vapour since the H₂O profile with NLC differs from that without NLC. In the
216 presence of NLC there is a reduction in water vapour mixing ratio (dehydration) between 83-
217 90 km, i.e. in the region where the saturation ratio of water vapour is larger than one. An
218 enhancement in water vapour (hydration) is observed at altitudes between 79-83 km, where the
219 saturation ratio of water vapour is smaller than one. An environment with a water vapour
220 saturation ratio larger than one is supersaturated, meaning ice particles can grow under these
221 conditions whereas a saturation ratio lower than one leads to ice sublimation. The degree of
222 saturation depends on the background atmosphere's H₂O concentration, and temperature. Ice
223 particles formation starts at higher altitudes, where the temperature is the lowest, and then they
224 sediment downward. During sedimentation, the ice particles grow by consuming H₂O from the
225 surrounding background, which decreases background H₂O concentration. Then they approach
226 a region with a saturation ratio smaller than one, where they sublimate, releasing the water
227 vapour. This is the so-called freeze-drying effect well discussed in a number of papers (Hervig
228 et al., 2003; Lübken et al., 2009; Bardeen et al., 2010). The results in Figure 4 illustrate the
229 freeze-drying effect described above and also indicate that the effects of NLC on H₂O are not
230 present below ~79 km and above ~97 km. This is the novelty of the results in Figure 4. This is
231 because the photochemical lifetime of water vapour below ~79 km becomes larger than
232 dynamical characteristic times, and distributions of water vapour become dynamically

233 determined. Above 97 km, the saturation ratio of water vapour is smaller than one;
234 consequently, there is no NLC formation and consequently no effect on water vapour.

235

236 **3.3. Effect of solar cycle-induced temperature and photolysis changes on water vapour** 237 **(H₂O)**

238

239 We investigate the temperature change between the solar minimum (1997) and maximum
240 (2002) due to solar irradiance variation and how these changes affect the H₂O profile. Different
241 model runs performed for this study are summarized in Table 1. The differences (solar
242 maximum - solar minimum) for H₂O and temperature profiles are shown in Figure 5 for three
243 model runs, namely E, F, and G. In run E, the solar cycle-induced temperature change and
244 photolysis influences H₂O concentration. In run F, only the temperature change caused by the
245 solar cycle affects the H₂O concentration, while in run G, only the photolysis caused by the
246 solar cycle affects the H₂O concentration (see Table 1). All of these runs are performed with
247 constant CO₂ and CH₄ concentrations to avoid the effects of increasing GHG concentrations on
248 temperature and H₂O profiles.

249 In model run F, Ly α is held constant in MIMAS, so the photolysis of H₂O is constant during
250 the solar cycle. However, Ly α (and other bands) varies in the LIMA model, so the background
251 temperature varies with the solar cycle. Therefore, the change in the H₂O profile during the
252 solar cycle is only due to the influence of the solar cycle on temperature and sequentially on
253 microphysical processes. Figure 5a shows that the temperature increases during solar maximum
254 compared to solar minimum through the entire altitude range (79-97 km). The difference of
255 temperature amounts to ~0.5-1.7 K with maximum values at ~95 km. During solar maximum,
256 increased solar irradiance leads to greater absorption of solar radiation in the MLT region by
257 molecular oxygen and water vapour, which heats the background atmosphere. Temperature

Fig. 5a

258 differences decrease as altitude decreases because the intensity of solar radiation decreases due
259 to atmospheric absorption by molecular oxygen and water vapour. The solar cycle effect in the
260 H₂O profile with NLC (blue line) differs significantly from that without NLC (yellow line).
261 Without NLC, the H₂O profile difference is nearly zero at all altitudes, indicating that the
262 temperature changes do not significantly affect the background H₂O profile in the absence of
263 NLC. With NLC, the H₂O profile difference is positive in the altitude range of 82-87 km and
264 slightly negative in the range from 79 to 82 km. The atmosphere is warmer during solar
265 maximum; therefore, the ice formation rate is lower during solar maximum. When the ice
266 formation rate decreases, the amount of water vapour consumed from the background
267 decreases; hence, more H₂O is left in the background during solar maximum compared to solar
268 minimum, resulting in a slightly positive response at NLC forming altitudes above 83 km.
269 Below that altitude, the slightly negative response is due to reduced ice formation in the
270 nucleation region during solar maximum, which decreases H₂O released at ice sublimation
271 altitudes. The positive difference peak at ~83 km is located near the bottom of the H₂O-saturated
272 zone. Ice formation/sublimation is more sensitive to an increase in background temperature at
273 this zone (where the degree of saturation is close to one) because at these altitudes the
274 background temperature is almost equal to the frost point temperature, so an increase in
275 background temperature critically changes the degree of saturation. The change of the
276 background temperature in a region where it is significantly lower than the frost point
277 temperature is not critical for the degree of saturation. Overall, the temperature variation due to
278 the solar cycle causes a positive H₂O response on the solar cycle at ice-formation altitudes and
279 a slightly negative response at ice-sublimation altitudes.

280 In model run G (Fig. 5b), we consider only the effect of solar cycle-induced Ly α variation on
281 water vapour photolysis. The background temperature is held constant. Photolysis of H₂O by
282 Ly α radiation molecules mainly produce atomic hydrogen (H) and hydroxyl (OH) in the upper
283 atmosphere (~90 %) and with less extent to O(¹D) with molecular hydrogen (~10 %). The

Fig. 5b

284 photolysis rate is higher during solar maximum due to the increased Ly α flux caused by the
285 increased solar activity. Without NLC, the difference in the H₂O profile is negative at all
286 altitudes (yellow line), indicating that the background H₂O is reduced during solar maximum
287 due to increased photolysis. Figure 5b shows that the negative response peaks at an altitude of
288 ~87.5 km. The solar cycle effect on the photolysis of H₂O decreases above 87.5 km because the
289 water vapour mixing ratio decreases with increasing altitude. The solar cycle variation of the
290 photolysis effect decreases below 87.5 km because the solar Ly α radiation intensity decreases.
291 With NLC (blue line), the H₂O difference between the solar maximum and the solar minimum
292 is essentially negative at ice sublimation altitudes (below ~83 km) and negligible at higher
293 altitudes (above ~85 km). This is due to the redistribution of the H₂O profile during NLC
294 formation (“freeze-drying”). During solar maximum, the background H₂O concentration
295 available for ice formation is reduced due to enhanced photolysis. The lower H₂O availability
296 during solar maximum results in lower ice formation and, thus, lower H₂O release during
297 sublimation, leading to lower hydration in the sublimation zone. For this reason, the solar cycle
298 variation of the photolysis effect is more pronounced at sublimation altitudes. Above 85 km,
299 the effect of photolysis, in the case with NLC, is minimal because of the lower availability of
300 H₂O due to dehydration by NLC.

301 Figure 5c shows a combination of both effects, namely the solar cycle-induced temperature
302 change and photolysis effects on H₂O. Without NLC (yellow line), the H₂O profile shows a
303 negative response at all altitudes, peaking at ~87.5 km similar to run G (Fig. 5b, yellow line).
304 We found that the variation of temperature has an almost negligible effect on the H₂O in the
305 absence of NLC (see Fig. 5a, yellow line), so the negative response of water vapour without
306 consideration of microphysical processes (yellow line on Fig. 5c) is mainly caused by the
307 photolysis effect. With NLC (Fig. 5c, blue line), the combined effect of temperature and
308 photolysis has a slightly positive response on water vapour in the ice formation zone (83-89km)
309 and a negative response in the ice sublimation zone (80-83km). The slightly positive response

Fig. 5c

310 is caused by the temperature modulation, and the negative response is primarily due to the
311 photolysis modulation throughout the solar cycle.

312 The study proves that the water vapour response to the solar cycle is affected by the re-
313 distribution of water in the presence of NLC. There may exist regions with positive correlation
314 of water vapour with Ly α when NLC formation occurs. Without NLC, the water vapour always
315 shows a negative correlation to the solar cycle. When comparing the effects of solar cycle
316 modulations of temperatures and photolysis on H₂O, the photolysis has a stronger effect on
317 water vapour, however, the variation of temperature induces a positive correlation of solar
318 irradiance and H₂O.

319

320 **4. Increasing greenhouse gases and reducing solar cycle**

321

322 This section examines how the increase in GHGs affects the H₂O response to the solar cycle.
323 To distinguish the GHG effects, we compared the model results with increasing CO₂ and CH₄
324 (Run A) to the model run with constant CO₂ and CH₄ (Run E). It is noted already that an
325 increasing CO₂ concentration leads to a cooling of the middle atmosphere, and an increase in
326 CH₄ concentration leads to an increase in H₂O concentration (see Sec.2 for details). In Figure
327 2, the concentration of CO₂ and CH₄ increase during the late period, and at the same time, the
328 peak of the Ly α flux decreases. In order to filter out the effect of reduced Ly α intensity, we
329 calculated the H₂O response profile per unit of Ly α ($\Delta H_2O / \Delta Ly\alpha$). Figure 6 shows the result
330 for the first (1997-2002, blue line) and the second period (2008-2014, orange line) for model
331 runs E (Fig. 6a) and A (Fig. 6b) respectively. These profiles show positive and negative
332 responses depending on altitude. Under the conditions of constant GHGs (run E) the sensitivity
333 of water vapour to Ly α does not change from the early to the late period (Fig. 6a). As expected,
334 for the case of growing methane and carbon dioxide (run A), the sensitivity of water vapour to

Fig. 6

335 Ly α increases during the late period (orange line, Fig. 6b) compared to the early period (blue
336 line, Fig. 6b). This is because an increase in CO₂ (and consequently temperature decrease) leads
337 to an intensification of microphysical processes, hence, to the increased freeze-drying. In
338 addition, increasing methane leads to more water vapour in the upper mesosphere, which also
339 leads to an increased water vapour variation with solar cycle.

340 To study the effect of a decreasing Ly α amplitude during the late period (2008-2014), we
341 calculated the ratio of water vapour absolute deviations between solar minimum and solar
342 maximum for the early and late period. The amplitude of Ly α variation is weaker during the
343 late period ($\sim 1.14 \cdot 10^{11}$ [phot.cm⁻²s⁻¹]/solar cycle) compared to the early period ($\sim 1.85 \cdot 10^{11}$
344 [phot.cm⁻²s⁻¹]/solar cycle). The intensity of Ly α during the late period solar maximum is
345 reduced by $\sim 40\%$ compared to the early period. As can be seen from Figure 7a the magnitudes
346 of positive and negative H₂O responses decreased during the late period for model runs with
347 constant GHGs (Run E). In Figure 6a, we found that the H₂O sensitivity to Ly α flux is the same
348 in the early and late periods for the model run with constant GHGs (Run E). Therefore, the
349 reduced response of H₂O during the late period in model run E (Fig. 7a) is only due to the
350 reduced solar Ly α variation. Comparing the late period H₂O response to the solar cycle from
351 model runs with constant GHG (Fig. 7a, orange line) to model runs with increasing GHG (Fig.
352 7b, orange line) suggests that both the positive and negative peak responses are enhanced by
353 increasing GHG concentration. Due to the increased solar Ly α flux and greenhouse gases, the
354 NLC and water vapour response is expected to increase during the current solar cycle 25, as the
355 Ly α radiance has already exceeded the peak value of the previous solar cycle 24.

Fig. 7

356

357 **5. Missing H₂O-solar cycle response**

358

359 A recent study by Hervig et al. (2019) reported a missing response in H₂O concentration on
360 solar cycle after 2005. In Figure 8, we compare our model results of H₂O anomaly with the
361 satellite observations. The H₂O response is averaged over the geometric altitudes of 80-85 km
362 at 68°N. For this comparison, we used MIMAS run A, where the increasing concentration of
363 GHG is considered. The satellite observations are shown in Figure 8 from HALOE, SOFIE,
364 and MLS according to Hervig et al. (2019). HALOE shows a strong negative response to Ly α
365 (-1.7 ppmv/solar cycle) during period 1, but in SOFIE and MLS the response is almost absent
366 (+0.2 ppmv/solar cycle) during period 2 (Hervig et al., 2019). For MIMAS, no clear H₂O-solar
367 cycle anti-correlation is noticed in the early period, but it was slightly positive in the late period
368 in agreement with SOFIE and MLS satellite observations. To investigate the H₂O response on
369 Ly α variation in more detail, we analysed the vertical H₂O response profile at geometric
370 altitudes similar to the satellite observations.

Fig. 8

371 Figure 9 shows the vertical profile of H₂O response in geometric altitudes for the model run
372 with constant GHGs (run E, Fig. 9a) and growing GHGs (run A, Fig. 9b). The magnitude of the
373 H₂O response at geometric altitudes (Fig. 9) differs from that at pressure altitudes (Fig.7). This
374 is because the geometric altitude of constant pressure levels is not constant and varies
375 throughout the solar cycle but also with time due to increasing GHG. Therefore, the magnitude
376 of the H₂O response differs when converted from pressure altitudes to geometric altitudes.
377 We focus on the 80-85 km geometric altitude range (Fig. 9. shaded region). There are positive
378 and negative H₂O response zones within this altitude range similar to Figure 7. We calculated
379 the average H₂O response over 80-85 km altitude range for MIMAS runs A and E is given in
380 Table 2. For the model run with growing GHGs (run A), the H₂O response averaged over an
381 altitude range of 80-85 km changed from -0.01 ppm/solar cycle in the early period to 0.10
382 ppm/solar cycle in the late period (see Table. 2). The H₂O response in the late period becomes
383 slightly positive for run A, consistent with the satellite observations of SOFIE and MLS (see
384 Fig. 8). The vertical profile of H₂O-solar cycle response clearly show that H₂O response to the

Fig. 9

385 solar cycle is not completely missing in the late period. The missing response in the MIMAS
386 H₂O as shown in Figure 8 occurred when averaging over the 80-85 km altitude range. Figure 9
387 demonstrates that the H₂O response shows nearly equal positive and negative responses within
388 the 80-85 km altitude range (shaded region). Therefore, averaging the response in this altitude
389 range becomes nearly zero, as the positive and negative responses cancel out each other. When
390 averaging over the altitude range of 80 to 82 km in the early period we receive H₂O response
391 of -0.71ppm/solar cycle and an anti-correlation between H₂O and Ly α . The results clearly
392 shows that the small solar cycle response in MIMAS is a consequence of averaging over an
393 altitude range of 80-85 km. It suggests that averaging H₂O response over an altitude range
394 containing positive and negative responses may not provide a detailed understanding of the
395 H₂O-solar cycle response.

396

397 **6. Conclusions**

398

399 In this study, we used our ice particle model MIMAS along with atmospheric dynamics model
400 LIMA to investigate the response of H₂O to the solar cycle from 1992-2018. We investigated
401 how NLC formation affects vertical H₂O profiles by running model simulations with and
402 without microphysics. NLC formations are shown to redistribute H₂O profiles by consuming
403 H₂O from the background at ice-forming altitudes (dehydration) and releasing it at ice-
404 sublimating altitudes (hydration) is known as the “freeze-drying” effect. To investigate the
405 missing solar cycle response in satellite observations reported by Hervig et al. (2019), we
406 divided the entire study period into an early (1992-2005) and late (2005-2018) period. We first
407 investigated how the Ly α variation affects the H₂O profile between solar minimum and
408 maximum in the early period. The solar Ly α variation affects the H₂O concentration at NLC
409 altitudes mainly in two ways: through the effect of temperature change and through the effect
410 of photolysis. To distinguish these two effects, we performed additional model simulations with

411 different background conditions (see Table 1). We found that the modulation of water vapour,
412 which comes through the temperature changes with solar cycle, causes a slight positive H₂O
413 response at ice-forming altitudes and a negative response at ice-sublimating altitudes. The solar
414 cycle photolysis effect has only negative responses on the H₂O profile, and this response
415 dominates at ice sublimation altitudes with NLC conditions. Our results for the case of
416 photolysis effect only are supported by previous simulations, which also suggest that freeze-
417 drying significantly reduces the potential effect of Ly α photolysis on H₂O above 82 km, while
418 the effect is enhanced at 80-82 km, where ice particles sublimate (von Zahn et al., 2004, Lübken
419 et al., 2009).

420 To the best of our knowledge, we have for the first time identified a positive response of water
421 vapour to Ly α variation in the MLT region which is due to microphysical processes. It was
422 assumed for a long time that water vapour only anti-correlates with the solar cycle at mesopause
423 altitudes (e.g. Sonnemann and Grygalashvyly, 2005; and references therein). We should note
424 that in the Martian atmosphere, where microphysical processes have a crucial role in water
425 vapour distributions through the entire atmosphere in all seasons (e.g. Shaposhnikov et al.,
426 2018), this effect may be important.

427 We have made a comparison between the model and satellite observations of the H₂O response
428 to the solar cycle, averaged over an altitude range of 80-85 km. The satellite observations from
429 HALOE show a strong anti-correlation to the solar cycle in the early period, but the model
430 shows a very small response in both the early and late periods. The vertical H₂O response
431 profiles from MIMAS show that within the 80-85 km altitude range, the positive and negative
432 responses are almost equal in magnitude and symmetric. Therefore, averaging the response over
433 this altitude range reduces the overall response in model, as positive and negative responses
434 cancel each other out.

435 We also investigated the role of increasing GHG on the H₂O-solar cycle response. From the
436 early to the late period, there are mainly two factors that affect the long-term H₂O solar cycle

437 response: increasing CO₂ and CH₄ concentrations and the lower intensity of the solar cycle (see
438 Figure 2). We found that increasing GHG concentration increased the H₂O response to Ly α .
439 The Ly α intensity during the late solar maximum decreased by 40% compared to the early solar
440 maximum. Therefore, the overall response of H₂O to the solar cycle is also decreased in the late
441 period. It should be noted that our results have limitations as they use constant dynamics for all
442 years. We are looking forward to a new gravity wave resolving model to investigate the effects
443 on changing dynamics due to changing GHGs and solar activity.

444

445 **Appendix**

446

447 **Data availability.** The satellite data shown in this paper are reproduced from the paper by
448 Hervig et al., 2019. Lyman- α data are available at <http://lasp.colorado.edu/lisird/lya/> from
449 LASP. The data utilized in this manuscript can be downloaded from [https://www.radar-
450 service.eu/radar/en/dataset/ArvFyujQbPGYfRqv?token=UEOfafmhOFFfWBRKONmZ](https://www.radar-service.eu/radar/en/dataset/ArvFyujQbPGYfRqv?token=UEOfafmhOFFfWBRKONmZ)

451

452 **Author contributions.** All authors contributed equally to this paper.

453 **Competing interests.**

454 **Acknowledgements.** We acknowledge the Mauna Loa records for CO₂ and CH₄ from
455 <http://www.esrl.noaa.gov/gmd/ccgg/>. This paper is partly supported by the TIMA project of the
456 BMBF research initiative ROMIC.

457

458 **References**

459 Berger, U. (2008). Modeling of middle atmosphere dynamics with LIMA. Journal of
460 Atmospheric and Solar-Terrestrial Physics, 70(8–9), 1170–1200.
461 <https://doi.org/10.1016/j.jastp.2008.02.004>

462

463 Berger, U., & Lübken, F. J. (2011). Mesospheric temperature trends at mid-latitudes in summer.
464 Geophysical Research Letters, 38(22). <https://doi.org/10.1029/2011GL049528>
465

466 Berger, U., & Lübken, F. J. (2015). Trends in mesospheric ice layers in the Northern
467 Hemisphere during 1961-2013. Journal of Geophysical Research, 120(21), 11,277-11,298.
468 <https://doi.org/10.1002/2015JD023355>
469

470 Berger, U., & von Zahn, U. (2002). Icy particles in the summer mesopause region: Three-
471 dimensional modeling of their environment and two-dimensional modeling of their transport.
472 Journal of Geophysical Research: Space Physics, 107(A11).
473 <https://doi.org/10.1029/2001JA000316>
474

475 Brasseur, G., and S. Solomon (2005), Aeronomy of the Middle Atmosphere
476

477 Compo, G. P., Whitaker, J. S., Sardeshmukh, P. D., Matsui, N., Allan, R. J., Yin, X., Gleason,
478 B. E., Vose, R. S., Rutledge, G., Bessemoulin, P., BroNnimann, S., Brunet, M., Crouthamel, R.
479 I., Grant, A. N., Groisman, P. Y., Jones, P. D., Kruk, M. C., Kruger, A. C., Marshall, G. J., ...
480 Worley, S. J. (2011). The Twentieth Century Reanalysis Project. In Quarterly Journal of the
481 Royal Meteorological Society (Vol. 137, Issue 654, pp. 1–28). John Wiley and Sons Ltd.
482 <https://doi.org/10.1002/qj.776>
483

484 DeLand, M. T., & Thomas, G. E. (2015). Updated PMC trends derived from SBUV data.
485 Journal of Geophysical Research, 120(5), 2140–2166. <https://doi.org/10.1002/2014JD022253>
486

487 DeLand, M. T., & Thomas, G. E. (2019). Evaluation of Space Traffic Effects in SBUV Polar
488 Mesospheric Cloud Data. *Journal of geophysical research. Atmospheres JGR*, 124(7), 4203–
489 4221. <https://doi.org/10.1029/2018JD029756>
490

491 DeLand, M. T., Shettle, E. P., Thomas, G. E., & Olivero, J. J. (2006). A quarter-century of
492 satellite polar mesospheric cloud observations. *Journal of Atmospheric and Solar-Terrestrial*
493 *Physics*, 68(1), 9–29. <https://doi.org/10.1016/J.JASTP.2005.08.003>
494

495 DeLand, M. T., Shettle, E. P., Thomas, G. E., & Olivero, J. J. (2003). Solar backscattered
496 ultraviolet (SBUV) observations of polar mesospheric clouds (PMCs) over two solar cycles.
497 *Journal of Geophysical Research: Atmospheres*, 108(8). <https://doi.org/10.1029/2002jd002398>
498

499 Fiedler, J., Baumgarten, G., Berger, U., Hoffmann, P., Kaifler, N., & Lübken, F. J. (2011). NLC
500 and the background atmosphere above ALOMAR. *Atmospheric Chemistry and Physics*,
501 11(12), 5701–5717. <https://doi.org/10.5194/acp-11-5701-2011>
502

503 Gadsden, M., & Schröder, W. (1989). Noctilucent Clouds. *Noctilucent Clouds*, 1–
504 12. doi:10.1007/978-3-642-48626-5_1
505

506 Garcia, R. R., Marsh, D. R., Kinnison, D. E., Boville, B. A., & Sassi, F. (2007). Simulation of
507 secular trends in the middle atmosphere, 1950-2003. *Journal of Geophysical Research*
508 *Atmospheres*, 112(9). <https://doi.org/10.1029/2006JD007485>
509

510 Garcia, R. R. (1989). Dynamics, Radiation, and Photochemistry in the Mesosphere’
511 Implications for the Formation of Noctilucent Clouds. In *JOURNAL OF GEOPHYSICAL*
512 *RESEARCH* (Vol. 94, Issue D12).

513

514 Hartogh, P., Sonnemann, G. R., Grygalashvyly, M., Song, L., Berger, U., & Lübken, F.-J.
515 (2010). H₂O measurements at ALOMAR over a solar cycle compared with model calculations
516 by LIMA. *Journal of Geophysical Research*, 115. <https://doi.org/10.1029/2009jd012364>

517

518 Hervig, M., McHugh, M., and Summers, M. E. (2003), Water vapor enhancement in the polar
519 summer mesosphere and its relationship to polar mesospheric clouds, *Geophys. Res. Lett.*, 30,
520 2041, doi:[10.1029/2003GL018089](https://doi.org/10.1029/2003GL018089), 20.

521

522 Hervig, M. E., Berger, U., & Siskind, D. E. (2016). Decadal variability in PMCs and
523 implications for changing temperature and H₂O in the upper mesosphere. *Journal of*
524 *Geophysical Research*, 121(5), 2383–2392. <https://doi.org/10.1002/2015JD024439>

525

526 Hervig, M. E., Siskind, D. E., Bailey, S. M., & Russell, J. M. (2015). The influence of PMCs
527 on water vapor and drivers behind PMC variability from SOFIE observations. *Journal of*
528 *Atmospheric and Solar-Terrestrial Physics*, 132, 124–134.
529 <https://doi.org/10.1016/j.jastp.2015.07.010>

530

531 Hervig, M. E., Siskind, D. E., Bailey, S. M., Merkel, A. W., DeLand, M. T., & Russell, J. M.
532 (2019). The Missing Solar Cycle Response of the Polar Summer Mesosphere. *Geophysical*
533 *Research Letters*, 46(16), 10132–10139. <https://doi.org/10.1029/2019GL083485>

534

535 Karagodin-Doyennel, A., Rozanov, E., Kuchar, A., Ball, W., Arsenovic, P., Remsberg, E.,
536 Jöckel, P., Kunze, M., Plummer, D. A., Stenke, A., Marsh, D., Kinnison, D., & Peter, T. (2021).

537 The response of mesospheric H₂O and CO to solar irradiance variability in models and obser-
538 vations. *Atmospheric Chemistry and Physics*, 21(1), 201–216. [https://doi.org/10.5194/acp-21-](https://doi.org/10.5194/acp-21-201-2021)
539 [201-2021](https://doi.org/10.5194/acp-21-201-2021).

540

541 Kiliani, J., 3-D Modeling of Noctilucent Cloud Evolution and Relationship to the Ambient At-
542 mosphere, *PhD thesis University Rostock*, [https://www.iap-kborn.de/fileadmin/user_up-](https://www.iap-kborn.de/fileadmin/user_upload/MAIN-abteilung/optik/Forschung/Doktorarbeiten/Kiliani-Diss-2014_s.pdf)
543 [load/MAIN-abteilung/optik/Forschung/Doktorarbeiten/Kiliani-Diss-2014_s.pdf](https://www.iap-kborn.de/fileadmin/user_upload/MAIN-abteilung/optik/Forschung/Doktorarbeiten/Kiliani-Diss-2014_s.pdf), 2014.

544

545 Lean, J. L., Rottman, G. J., Kyle, H. L., Woods, T. N., Hickey, J. R., and Puga, L. C.: Detection
546 and parameterization of variations in solar mid- and near-ultraviolet radiation (200–400 nm), *J.*
547 *Geophys. Res.*, 102, 29939–29956, doi:10.1029/95GL03093, 1997.

548

549 Lübken, F. J., Baumgarten, G., & Berger, U. (2021). Long term trends of mesospheric ice layers:
550 A model study. *Journal of Atmospheric and Solar-Terrestrial Physics*, 214.
551 <https://doi.org/10.1016/j.jastp.2020.105378>

552

553 Lübken, F. J., Berger, U., & Baumgarten, G. (2009). Stratospheric and solar cycle effects on
554 long-term variability of mesospheric ice clouds. *Journal of Geophysical Research Atmospheres*,
555 114(21). <https://doi.org/10.1029/2009JD012377>

556

557 Lübken, F. J., Berger, U., & Baumgarten, G. (2013). Temperature trends in the midlatitude
558 summer mesosphere. *Journal of Geophysical Research Atmospheres*, 118(24), 13,347-13,360.
559 <https://doi.org/10.1002/2013JD020576>

560

561 Lübken, F. J., Berger, U., & Baumgarten, G. (2018). On the Anthropogenic Impact on Long-
562 Term Evolution of Noctilucent Clouds. *Geophysical Research Letters*, 45(13), 6681–6689.
563 <https://doi.org/10.1029/2018GL077719>
564

565 Machol, J., Snow, M., Woodraska, D., Woods, T., Viereck, R., & Coddington, O. (2019). An
566 Improved Lyman-Alpha Composite. *Earth and Space Science*, 6(12), 2263–2272.
567 <https://doi.org/10.1029/2019EA000648>.
568

569 Marsh, D. R., Mills, M. J., Kinnison, D. E., Lamarque, J. F., Calvo, N., & Polvani, L. M. (2013).
570 Climate change from 1850 to 2005 simulated in CESM1(WACCM). *Journal of Climate*, 26(19),
571 7372–7391. <https://doi.org/10.1175/JCLI-D-12-00558.1>
572

573 Medvedev, A. S., & Klaassen, G. P. (2000). Parameterization of gravity wave momentum
574 deposition based on nonlinear wave interactions: basic formulation and sensitivity tests. *Journal*
575 *of Atmospheric and Solar-Terrestrial Physics*, 62. www.elsevier.nl/locate/jastp
576

577 Roble, R. and Dickinson, R. (1989) How Will Changes in Carbon Dioxide and Methane Modify
578 the Mean Structure of the Mesosphere and Thermosphere? *Geophysical Research Letters*, 16,
579 1441-1444. <https://doi.org/10.1029/GL016i012p01441>
580

581 Sonnemann, G. R., & Grygalashvyly, M. (2005). Solar influence on mesospheric water vapor
582 with impact on NLCs. *Journal of Atmospheric and Solar-Terrestrial Physics*, 67(1–2), 177–
583 190. <https://doi.org/10.1016/j.jastp.2004.07.026>
584

585 Shaposhnikov, D. S., Rodin, A. V., Medvedev, A. S., Fedorova, A. A., Kuroda, T., & Hartogh,
586 P. (2018). Modeling the hydrological cycle in the atmosphere of Mars: Influence of a bimodal

587 size dis-tribution of aerosol nucleationparticles.Journal of GeophysicalResearch: Planets,123,
588 508–526.<https://doi.org/10.1002/2017JE005384>

589

590 Shettle, E. P., DeLand, M. T., Thomas, G. E., & Olivero, J. J. (2009). Long term variations in
591 the frequency of polar mesospheric clouds in the Northern Hemisphere from SBUV.
592 Geophysical Research Letters, 36(2). <https://doi.org/10.1029/2008GL036048>

593

594 Siskind, D. E., Stevens, M. H., Hervig, M. E., & Randall, C. E. (2013). Recent observations of
595 high mass density polar mesospheric clouds: A link to space traffic? Geophysical Research
596 Letters, 40(11), 2813–2817. <https://doi.org/10.1002/grl.50540>

597

598 Thomas, G. E. (1996). IS THE POLAR MESOSPHERE THE MINER’S CANARY OF
599 GLOBAL CHANGE? In Adv. Space Res (Vol. 18, Issue 3).

600

601 Thomas, G. E., & Olivero, J. (2001). Noctilucent clouds as possible indicators of global change
602 in the mesosphere. Advances in Space Research, 28(7), 937–946.
603 [https://doi.org/10.1016/S0273-1177\(01\)80021-1](https://doi.org/10.1016/S0273-1177(01)80021-1)

604

605 von Zahn, U., & Berger, U. (2003). Persistent ice cloud in the midsummer upper mesosphere
606 at high latitudes: Three-dimensional modeling and cloud interactions with ambient H₂O.
607 Journal of Geophysical Research: Atmospheres, 108(8). <https://doi.org/10.1029/2002jd002409>

608

609 von Zahn, U., Baumgarten, G., Berger, U., Fiedler, J., & Hartogh, P. (2004). Atmospheric
610 Chemistry and Physics Noctilucent clouds and the mesospheric water vapour: the past decade.
611 In Atmos. Chem. Phys (Vol. 4). www.atmos-chem-phys.org/acp/4/2449/

612

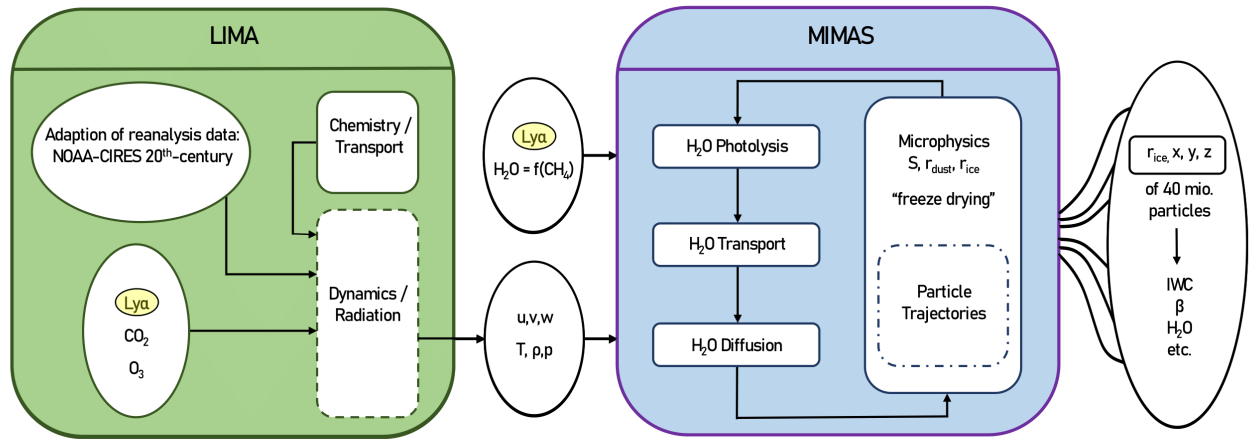
613 Woods, T. N., Tobiska, W. K., Rottman, G. J., & Worden, J. R. (2000). Improved solar Lyman
614 α irradiance modeling from 1947 through 1999 based on UARS observations. In Journal of
615 Geophysical Research: Space Physics (Vol. 105, Issue A12, pp. 27195–27215). Blackwell
616 Publishing Ltd. <https://doi.org/10.1029/2000ja000051>

617

618 **Figures**

619

620 Figure 1. Sketch of the LIMA (green) and MIMAS (blue) models (from Lübken et al., 2021)



621

622

623

624

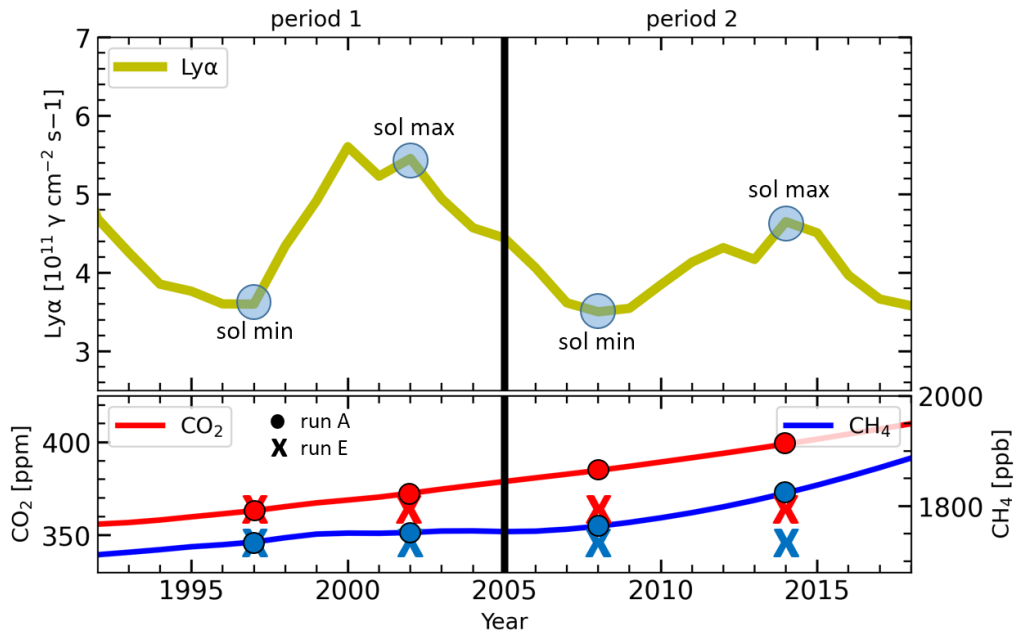
625

626

627

628

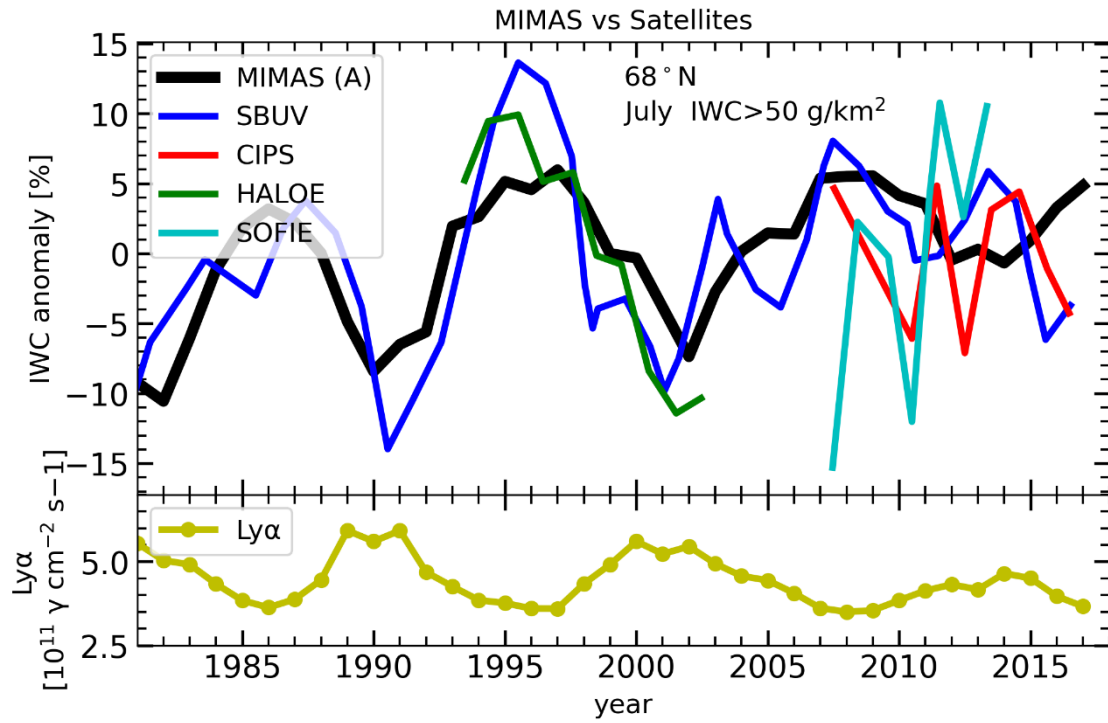
629 Figure 2. Time series of solar $\text{Ly}\alpha$, CO_2 , and CH_4 for 1992-2018. The corresponding $\text{Ly}\alpha$,
 630 CO_2 , and CH_4 values for the solar cycle maximum and minimum years used for this study are
 631 marked. The CO_2 and CH_4 values for run A are represented with dots, and for run E with
 632 crosses. The study period is divided into period 1 as early (1992-2005) and period 2 as late
 633 (2005-2018).



634

635

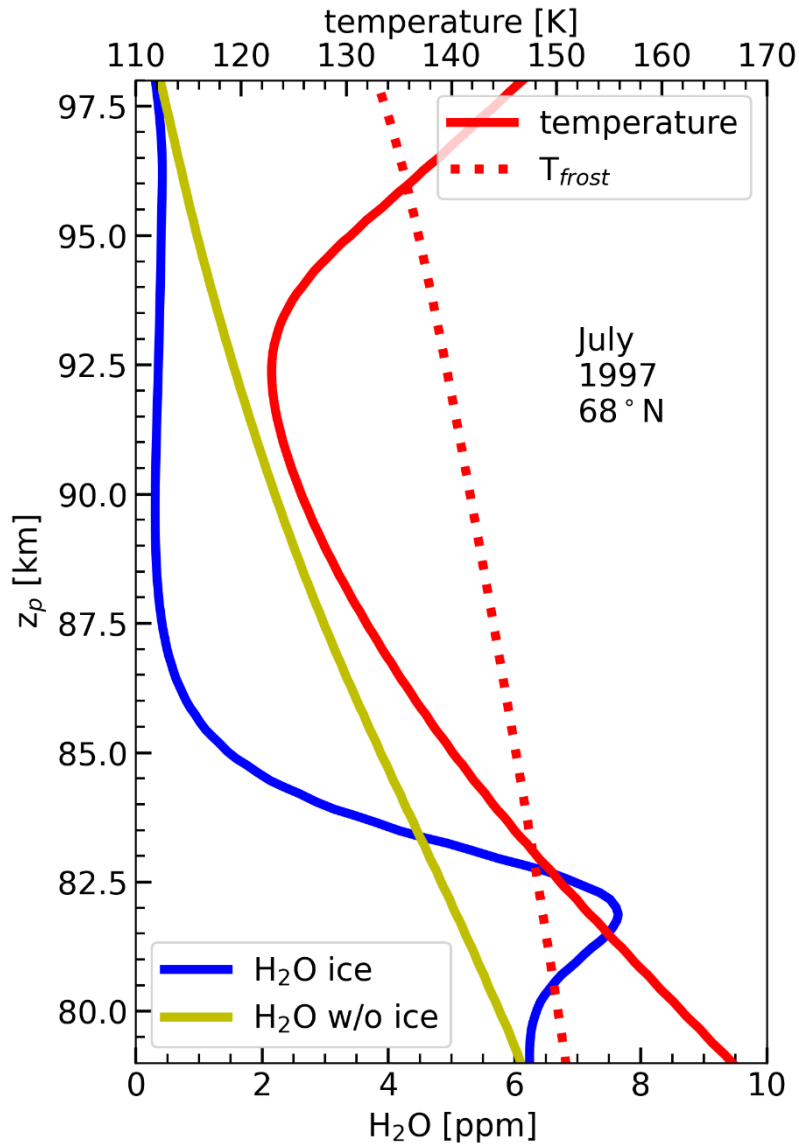
636 Figure 3. Time series of July mean IWC anomalies at 68°N from model and satellites based on
637 Hervig et al., (2019). Anomalies for each data set are calculated as the difference from their
638 long-term mean. To reduce year to year variability, the time series of SBUV and HALOE are
639 smoothed using the sliding average method of window size 3. Ly α -solar cycle modulation is
640 shown in the bottom panel.



641

642

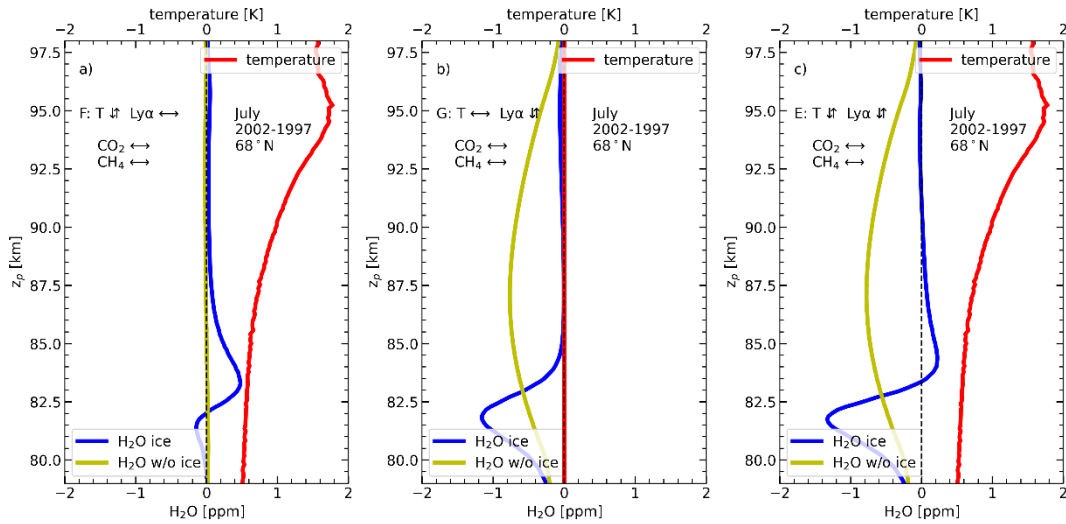
643 Figure 4. Zonally and monthly averaged H₂O and temperature profile for July at 68°N from
644 MIMAS with and without NLCs. The red dotted line represents frost point temperature. The
645 blue lines show the background H₂O concentration with NLC, and the yellow lines show the
646 H₂O concentration without NLC.



647

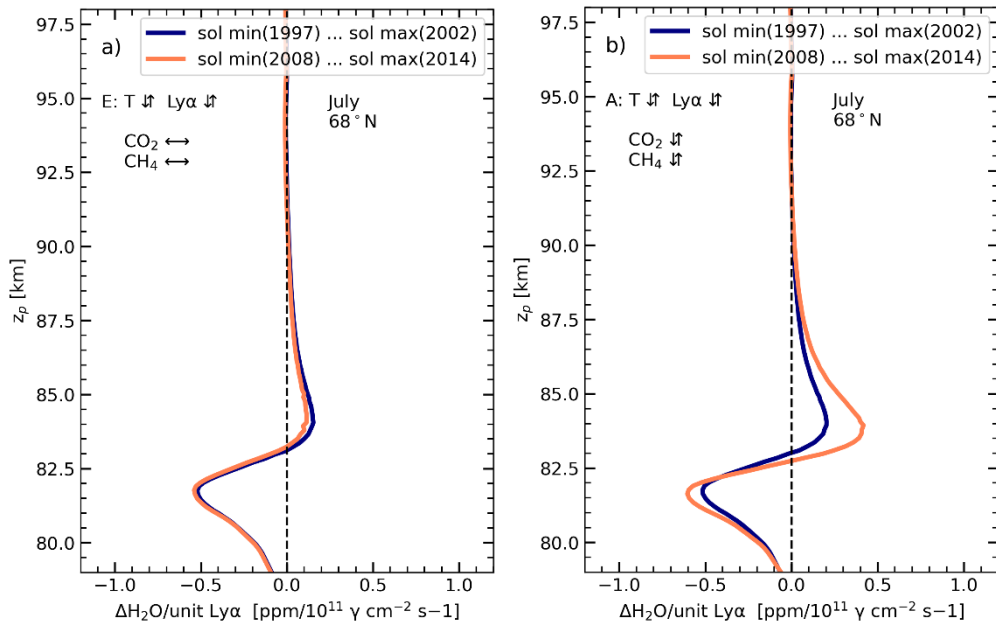
648

649 Figure 5. The difference in profiles between solar maximum (2002) and minimum (1997) for
 650 July mean H₂O and temperatures. The blue and yellow lines represent NLC and non-NLC
 651 conditions. In all cases, CO₂ and CH₄ values are constant corresponding to 1997. (a) Run F:
 652 only temperature change effects on H₂O, (b) Run G: only Photolysis change effect on H₂O, (c)
 653 Run E: both temperature change and photolysis change effects on H₂O



654

655 Figure 6. H₂O-response per unit Ly α variations in July at 68°N during the years between solar
 656 minimum and maximum in the early (1997 to 2002) and late (2008 to 2014) periods. (a)
 657 MIMAS model run E with constant CO₂ and CH₄, (b) MIMAS model run A with varying CO₂
 658 and CH₄.



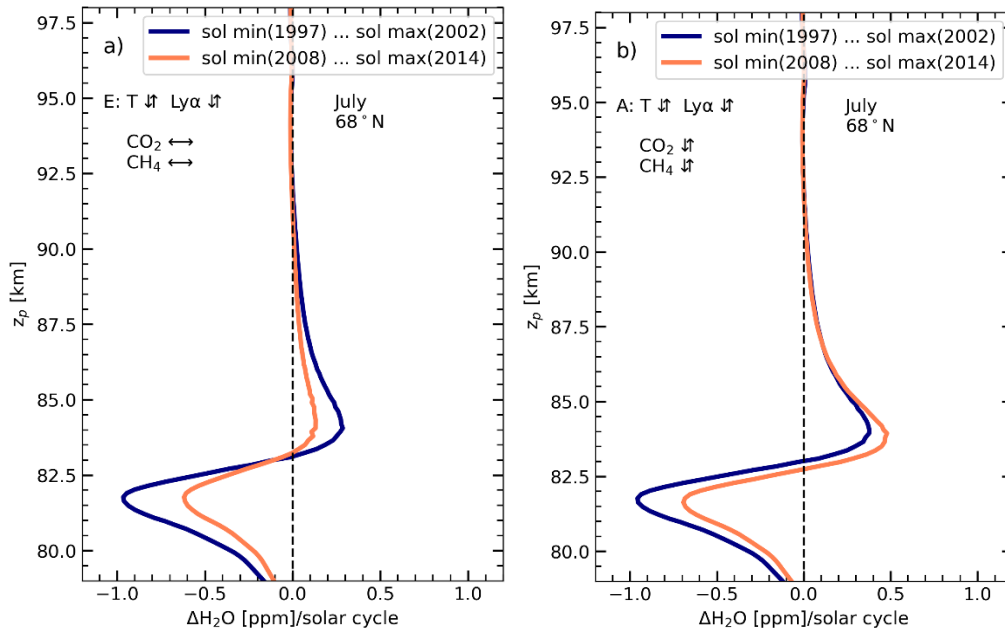
659

660

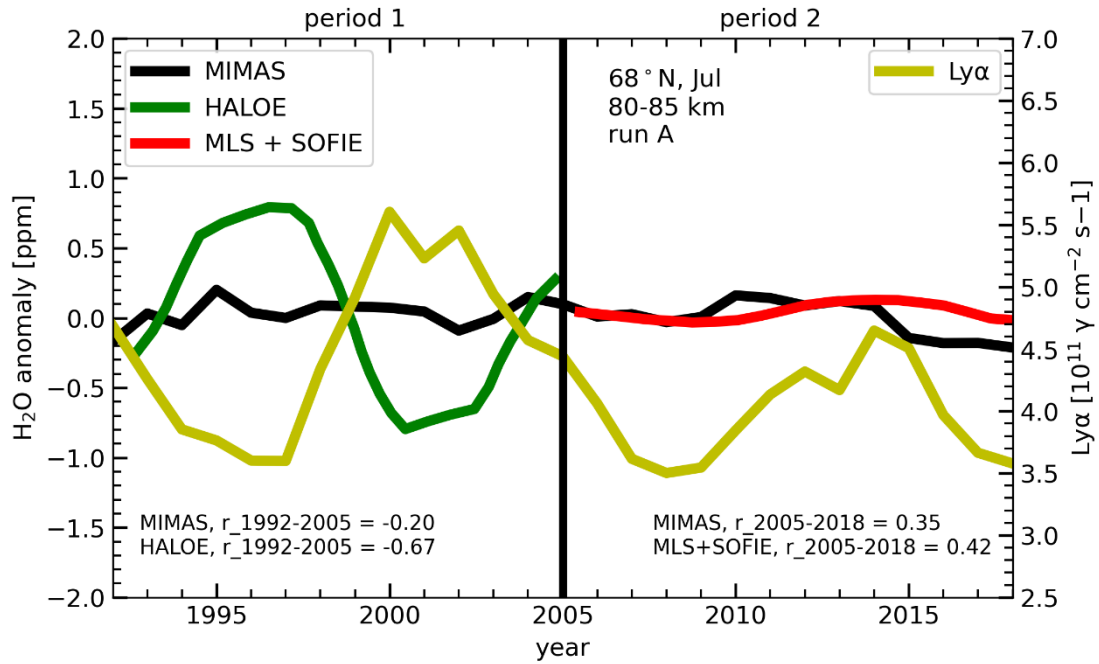
661

662 Figure 7. H₂O-response to absolute solar cycle Ly α variations in July at 68°N during the years
663 between solar minimum and maximum in the early (1997 to 2002) and late (2008 to 2014)
664 periods. (a) MIMAS model run E with constant CO₂ and CH₄, (b) MIMAS model run A with
665 varying CO₂ and CH₄.

666



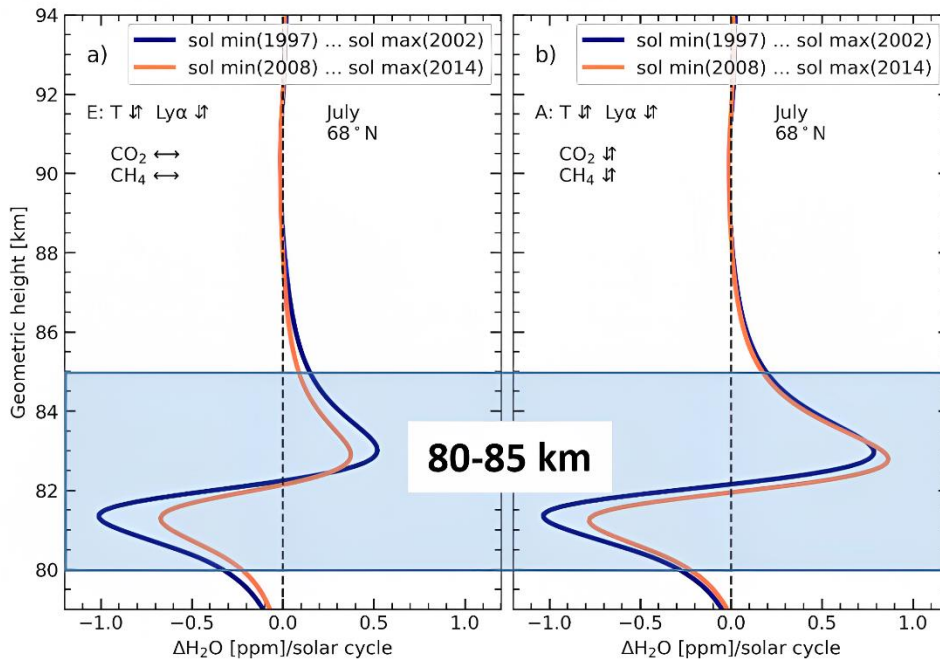
669 Figure 8. Time series of Ly α and H₂O anomalies as monthly averages for July at 68°N for the
 670 altitude range of 80 km to 85 km from MIMAS run A and satellites (HALOE and the composite
 671 data (MLS and SOFIE)). Satellite observations are according to Hervig et al., 2019. The H₂O-
 672 Ly α correlation is calculated for the early and late periods (see inlet).



673

674

675 Figure 9. H₂O-response to absolute solar cycle Ly α variations in July at 68°N during the years
 676 between solar minimum and maximum in the early (1997 to 2002) and late (2008 to 2014)
 677 periods represented in geometric altitudes. The shaded region represents the altitudes range
 678 used for calculating an average solar cycle response. (a) MIMAS model run E with constant
 679 CO₂ and CH₄, (b) MIMAS model run A varying CO₂ and CH₄.



680
 681
 682
 683
 684
 685
 686
 687
 688
 689
 690
 691
 692
 693

694 **Tables**

695 Table 1. MIMAS simulations were carried out under different background conditions. The
 696 horizontal arrow stands for constant values for the given year; the vertical arrow is for varying
 697 parameters. How Ly α affects H₂O is given for each run in the last column.

698

	LIMA		MIMAS		
Model run	CO₂	Lyα T effect	CH₄	Lyα photolysis effect	Water vapour solar cycle response affected by
A	↓	↓	↓	↓	<ul style="list-style-type: none"> • Temperature change (Lyα + CO₂) • Photo dissociation • Varying CH₄ (H₂O source)
E	↔ 1997	↓	↔ 1997	↓	<ul style="list-style-type: none"> • Temperature change • Photo dissociation
F	↔ 1997	↓	↔ 1997	↔ 1997	<ul style="list-style-type: none"> • Temperature change
G	↔ 1997	↔ 1997	↔ 1997	↓	<ul style="list-style-type: none"> • Photo dissociation

699

700

701

702

703

704 Table 2. The solar cycle H₂O response averaged over 80-85 km geometric altitude at 68°N
705 for model runs A and E.

706

Model run	ΔH₂O (ppm)/solar cycle (80-85km)	
	Early period	Late period
MIMAS with constant CO₂ and CH₄ (run E)	-0.11	-0.06
MIMAS with increasing CO₂ and CH₄ (run A)	-0.01	0.10

707

708

709

710